

# Crustal thickness and $V_P/V_S$ variations in the Grenville orogen (Ontario, Canada) from analysis of teleseismic receiver functions

David W. Eaton\*, Savka Dineva, Robert Mereu

*Department of Earth Sciences, University of Western Ontario, London, Ontario, Canada N6A 5B7*

Received 17 January 2005; accepted 4 January 2006

Available online 19 April 2006

## Abstract

We have developed a simple semblance-weighted stacking technique to estimate crustal thickness and average  $V_P/V_S$  ratio using teleseismic receiver functions. We have applied our method to data from 32 broadband seismograph stations that cover a  $700 \times 400 \text{ km}^2$  region of the Grenville orogen, a 1.2–0.98 Ga Himalayan-scale collisional belt in eastern North America. Our seismograph network partly overlaps with LITHOPROBE and other crustal refraction surveys. In 8 out of 9 cases where a crustal-refraction profile passes within 30 km of a seismograph station, the two independent crustal thickness estimates agree to within 7%. Our regional crustal-thickness model, constructed using both teleseismic and refraction observations, ranges between 34.0 and 52.4 km. Crustal-thickness trends show a strong correlation with geological belts, but do not correlate with surface topography and are far in excess of relief required to maintain local isostatic equilibrium. The thickest crust ( $52.4 \pm 1.7 \text{ km}$ ) was found at a station located within the 1.1 Ga mid-continent (failed) rift. The Central Gneiss Belt, which contains rocks exhumed from deep levels of the crust, is characterized by  $V_P/V_S$  ranging from 1.78 to 1.85. In other parts of the Grenville orogen,  $V_P/V_S$  is found to be generally less than 1.80. The thinnest crust (34.5–37.0 km) occurs northeast of the 0.7 Ga Ottawa–Bonnechere graben and correlates with areas of high intraplate seismicity.

© 2006 Elsevier B.V. All rights reserved.

**Keywords:** Grenville orogen; Crustal thickness;  $V_P/V_S$  ratio; Teleseismic receiver functions

## 1. Introduction

The 1.2–0.98 Ga Grenville orogeny was one of the most extensive mountain-building episodes in Earth history. The orogen is exposed primarily in a  $2000 \times 500 \text{ km}^2$  region along the southeastern edge of the Canadian shield, but correlative crustal units underlie a large portion of the U.S. mid-continent, and also occur in parts of Scandinavia, Australia, Africa and Antarctica (Karlstrom et al., 1999). The scale and tectonic

architecture of the Grenville orogen resemble the modern Alpine–Himalayan orogen, suggesting that it formed as the result of broadly similar continent–continent collisional processes (Carr et al., 2000). Several recent tectonic models also emphasize the pre-collisional history of the orogen, during which an Andean-style convergent margin persisted for almost 800 Ma along the southeastern margin of the North-American protocontinent, Laurentia (Rivers, 1997).

The Moho is a first-order geological discontinuity that separates crustal rocks from denser underlying lithospheric mantle material. The depth to the Moho is highly variable beneath modern mountain belts, with crustal thicknesses as great as 80 km beneath high

\* Corresponding author. Current address: Dublin Institute for Advanced Studies, 5 Merrion Square, Dublin 2, Ireland.

E-mail address: [deaton@uwo.ca](mailto:deaton@uwo.ca) (D.W. Eaton).

orogenic plateaus such as Tibet and the Altiplano, adjacent to areas of more normal continental crustal thickness (~35–40 km; Mooney et al., 1998). In the Grenville orogen, few vestiges of mountainous relief are preserved at the surface, but significant variations in crustal thickness have been documented by a number of large-scale refraction experiments that have been carried out across the region since the 1950s (Table 1). In the first experiment in this region, Hodgson (1953) placed recording instruments along a line in northern Ontario and derived values of 35.5 km for crustal thickness, 6.25 km/s for  $P_g$  velocity and 8.18 km/s for  $P_n$  velocity. These measurements stand to this day as representative values for the Canadian Shield.

In 1992, LITHOPROBE carried out a major seismic refraction experiment that crossed the Grenville Front on two transects. Over 40 drilled shot points were used, each recorded by over 400 instruments from the USGS and GSC. The large number of shots and receivers enabled researchers to analyze the data using tomographic techniques. For example, Winardhi and Mereu (1997) obtained a velocity model containing lateral velocity variations of up to 0.2 km/s in the upper crust between the Grenville and Superior Provinces. Their study confirmed that there is a major Moho trough to the south of the Grenville Front, as was found in previous studies of profiles across the Front (Mereu and Jobidon, 1971; Mereu et al., 1986). In a subsequent analysis of this data-set, Mereu (2000) used a combination of both  $P$ - and  $S$ -wave arrivals to compute Poisson's ratio along all of the profiles from measurements of the compressional-to-shear velocity ratio ( $V_p/V_s$ ), by taking the ratio

of the  $P_g$  arrival time to the  $S_g$  time (or  $PmP$  to  $SmS$  times for offsets greater than ~150 km) for each trace. It can be easily shown that this approach yields an accurate measurement of average  $V_p/V_s$  along the ray path, even for variable crustal velocity field.

Zhu and Kanamori (2000) have developed a simple technique to estimate average crustal thickness and  $V_p/V_s$  directly from teleseismic receiver functions. Their method provides robust “point” estimates of Moho depth and  $V_p/V_s$  by exploiting strong Moho phases that typically dominate the initial part (~25 s) of a receiver-function record. By stacking several modes of crustal reverberations, their method is largely insensitive to uncertainties in crustal velocity. Since the receiver-function technique involves passive recording of distant earthquakes, it provides a relatively inexpensive way to obtain crustal thickness and  $V_p/V_s$  information over a large area.

The advent of the POLARIS broadband seismograph network since 2001 (Atkinson et al., 2003) has provided unprecedented spatial coverage of the Grenville orogen in Ontario. In this paper, we use a modified form of Zhu and Kanamori's method to map Moho depth and crustal  $V_p/V_s$  ratio. Our study area (Fig. 1) covers the southwestern part of the Grenville Province and adjacent parts of the orogen where the Precambrian crust is buried beneath 0–2 km of Paleozoic sedimentary rocks. Taking into consideration the full extent of Grenvillian crust in North America, our investigation can be considered as centrally located with respect to the orogen as a whole.

## 2. Method

Teleseismic receiver functions are waveforms constructed using three-component recordings of  $P$ -arrivals from distant earthquakes, usually by deconvolving vertical ground-motion from radial and transverse horizontal ground motions (Langston, 1977; Owens et al., 1984; Bostock and Cassidy, 1995; Eaton and Hope, 2003). Analysis of receiver functions is a well-established method to image the structure of the crust and upper mantle beneath a recording station. Receiver function waveforms are typically characterized by a series of discrete pulses, produced mainly by  $S$ -wave scattering from subsurface discontinuities in elastic properties. In this study, we compute the time-domain radial receiver function  $f(t)$  using a simple frequency-domain deconvolution method:

$$f(t) = \int \frac{R(\omega)}{Z'(\omega)} e^{-\frac{(\omega-\omega_0)^2}{\sigma^2}} e^{i\omega t} d\omega, \quad (1)$$

Table 1  
Previous seismic refraction experiments in the study region

Location	Year	References
Northern Ontario	1953	Hodgson (1953)
Lake Superior	1963	Berry and West (1966); Smith et al. (1966)
Central Quebec	1968	Mereu and Jobidon (1971); Berry and Fuchs (1973)
Gravity Low		
The Ottawa Graben – Grenville Front	1982	Mereu et al. (1986)
Kapuskasing Structure	1984	Boland and Ellis (1989)
Great Lakes (GLIMCE)	1986	Green et al. (1988); Mereu et al. (1991)
Eastern Ontario – New York State	1988	Hughes and Luetgert (1992); Zelt et al. (1994); Musacchio et al. (1997)
Abitibi–Grenville (LITHOPROBE)	1992	Grandjean et al. (1995); Long and Salisbury (1996); Winardhi and Mereu (1997); White et al. (2000); Mereu (2000)

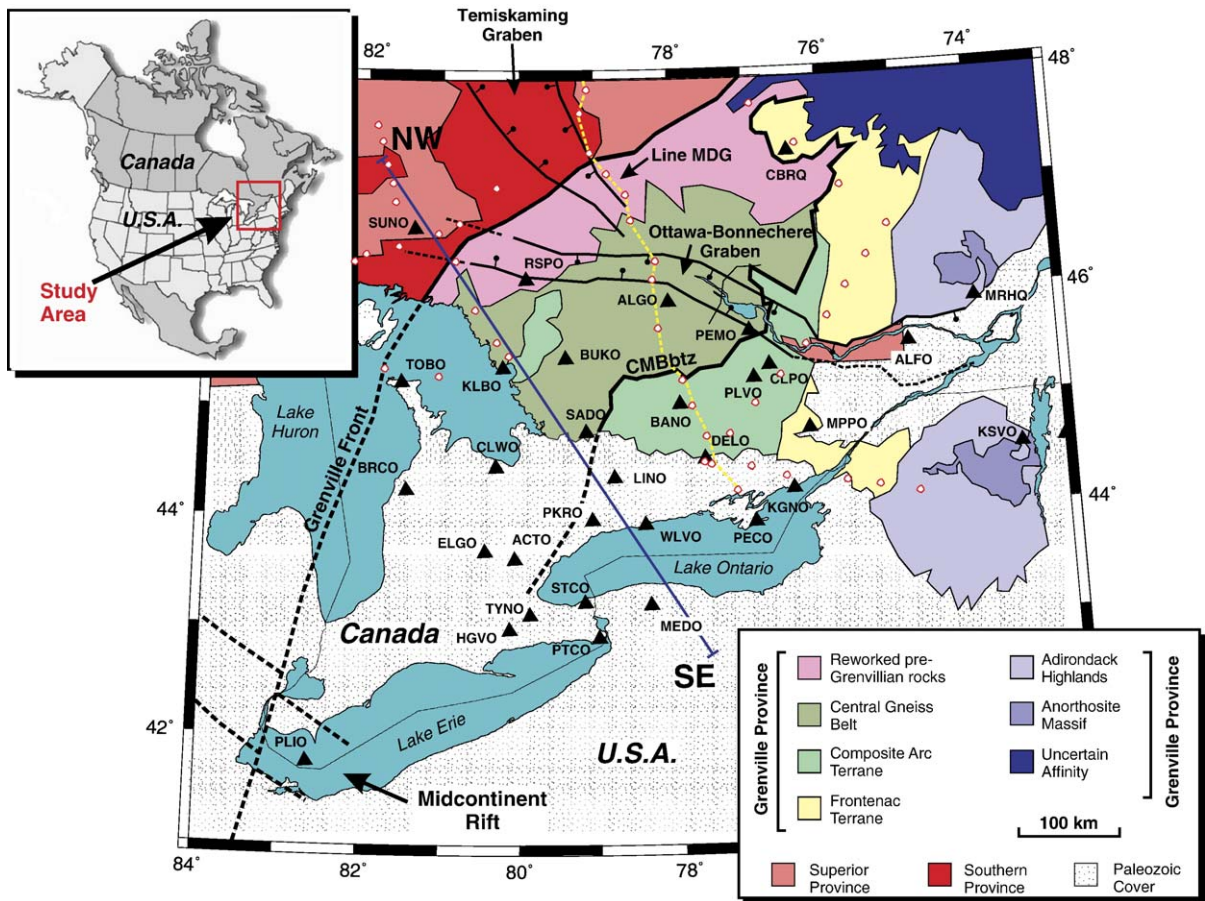


Fig. 1. Simplified geological map of the lower Great Lakes region (after Ludden and Hynes, 2000). Black triangles represent broadband three-component seismograph stations used in this study. Small white circles show locations where crustal thickness and  $V_P/V_S$  are available from published refraction experiments. NW and SE mark the location of the profile in Fig. 7. Line MDG shows the location of the 1991 LITHOPROBE refraction line (see Fig. 10). CMBbtz denotes Central Metasedimentary belt boundary tectonic zone (after O'Dowd et al., 2004).

where  $R(\omega)$  is the Fourier transform of the radial-component waveform,  $r(t)$ .  $Z'(\omega)$  serves as a first-order estimate of the source spectrum, and is given by

$$Z'(\omega) = Z(\omega) \quad \text{if} \quad |Z(\omega)| > c \max(|Z(\omega)|) \\ = c \max(|Z(\omega)|) \quad \text{otherwise,} \quad (2)$$

where  $Z(\omega)$  is the transform of the vertical-component waveform, and  $c$  is a so-called water-level parameter introduced to stabilize the deconvolution by suppressing “holes” in the spectrum. Noise is further reduced by applying a Gaussian-type band-pass filter, parameterized by a centre frequency,  $\omega_0$ , and a filter width  $\sigma$ .

Because of the large velocity contrast at the crust–mantle boundary, phases associated with the Moho tend to be prominent in receiver functions. We label the receiver-function arrivals for the Moho using the

notation of Bath and Steffanson (1966); in this notation, the incident upgoing wave at the Moho and downgoing reflected crustal travel paths are denoted by uppercase letters, whilst upgoing crustal travel paths are denoted by lowercase letters. Thus, for example,  $PpPs$  represents an incident  $P$  wave that is transmitted at the Moho as an upgoing  $P$  wave, reflected downwards at the surface and then converted to an upgoing  $S$ -wave at the Moho.

A set of synthetic receiver functions spanning an epicentral distance range of  $30^\circ - 90^\circ$  is shown in Fig. 2a. The full-waveform synthetic seismograms used to compute the receiver functions were obtained using the viscoelastic matrix formulation of Wang (1999), based on a crustal velocity–density model for the Ontario region (Fig. 2b). The velocity model (Table 2) was determined from local earthquake travel time analysis (Dineva et al., 2004). The amplitude of the strong initial

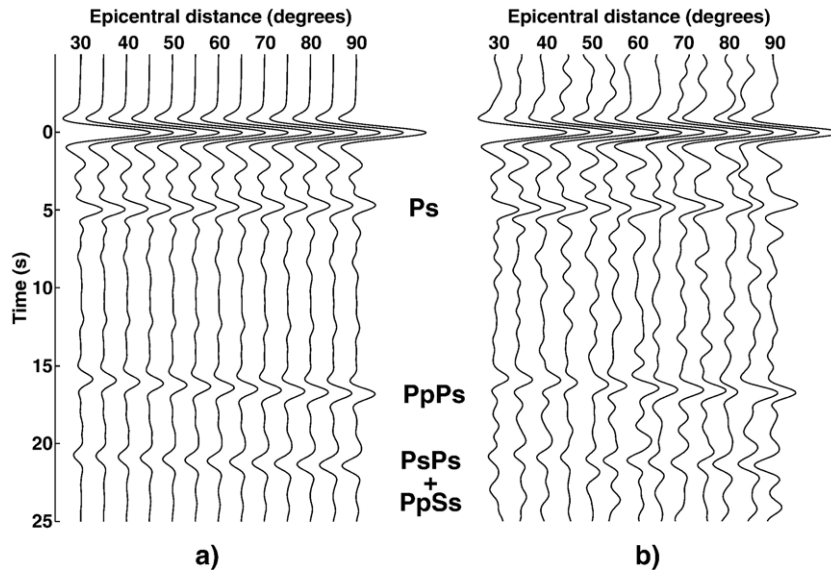


Fig. 2. Receiver functions obtained from synthetic seismograms, computed using modified Thompson–Haskell matrix method of Wang (1999). Crustal velocity–density model is given in Table 1. All layers were assigned quality factors  $Q_P=Q_S=1000$ . Seismograms were computed for slowness values equivalent to a range of epicentral distances from  $30^\circ$  to  $90^\circ$ , with focal depth of 100 km. (a) Noise-free synthetic seismograms; (b) synthetic seismograms with 10% noise added. Receiver functions have been scaled so that each trace has the same maximum amplitude.

phase at  $t=0$ , often referred to as the  $Pp$  arrival, is a measure of the zero-lag correlation between the radial and vertical components. The next strong phase at  $t \sim 5$  s represents the  $Ps$  converted phase from the Moho. The arrival time of this phase is equal to the time-separation between  $Pp$  and  $Ps$ , given by

$$t_{Ps} = H \left[ \sqrt{\frac{1}{V_S^2} - p^2} - \sqrt{\frac{1}{V_P^2} - p^2} \right], \quad (3)$$

where  $H$  is the thickness of the crust,  $V_P$  and  $V_S$  represent average crustal velocities and  $p$  is the ray parameter of the incident wave. The arrival time for the next prominent crustal phase,  $PpPs$ , is given by

$$t_{PpPs} = H \left[ \sqrt{\frac{1}{V_S^2} - p^2} + \sqrt{\frac{1}{V_P^2} - p^2} \right]. \quad (4)$$

This is followed by a composite arrival, which represents the net response of two kinematically equivalent

phases  $PpSs$  and  $PsPs$ . The arrival time for this phase is given by

$$t_{PsPs+PpSs} = 2H \sqrt{\frac{1}{V_S^2} - p^2}. \quad (5)$$

Given a priori knowledge of crustal velocity and thickness, the arrival times of these phases can be calculated easily, since  $p$  can be determined using a standard Earth model such as IASP91 (Kennett and Engdahl, 1991) provided that the source depth ( $h$ ) and epicentral distance ( $\Delta$ ) are known. Conversely, by measuring  $t_{Ps}$ ,  $t_{PpPs}$  and  $t_{PsPs+PpSs}$  it is possible, in principle, to solve this nonlinear system for the three unknown quantities  $H$ ,  $V_P$  and  $V_S$  (Zandt et al., 1995; Zandt and Ammon, 1995). In practice, these arrival times are relatively insensitive to  $P$ -wave velocity (Zhu and Kanamori, 2000). It is therefore common to use an assumed  $V_P$  value and solve for  $H$  and the ratio  $V_P/V_S$  (hereinafter denoted by  $\kappa$ ). This procedure is illustrated in Fig. 3, which shows the loci of  $H$  and  $\kappa$  values associated with ray theoretical values of  $t_{Ps}$ ,  $t_{PpPs}$  and  $t_{PsPs+PpSs}$  for the  $\Delta=60^\circ$  synthetic receiver function in Fig. 2a. As expected, these loci of  $H$  and  $\kappa$  values, or kinematic curves, intersect at the value of  $H$  and  $\kappa$  used to generate the synthetic seismograms.

Zhu and Kanamori (2000) have developed an efficient stacking technique to estimate  $H$  and  $\kappa$ . Their method has the advantage over direct solution of the

Table 2  
Crustal velocity–density model for Ontario

Depth (km)	$V_P$ (km/s)	$V_S$ (km/s)	$V_P/V_S$ ( $\kappa$ )	Density (g/cm <sup>3</sup> )
0	6.00	3.47	1.729	2.65
5	6.34	3.66	1.732	2.75
15	6.44	3.72	1.731	2.90
30	6.59	3.81	1.730	3.00
40	8.10	4.68	1.731	3.30
50	8.25	4.72	1.748	3.35



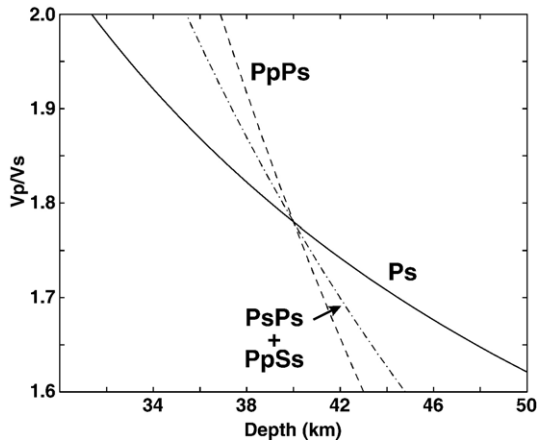


Fig. 3. Kinematic curves showing loci of  $(H, \kappa)$  values that correspond to  $t_{Ps}$ ,  $t_{PpPs}$  and  $t_{PsPs+PpSs}$  for the  $\Delta=60^\circ$  synthetic receiver function in Fig. 2a.

system of Eqs. (3)–(5) that it is not necessary to determine  $t_{Ps}$ ,  $t_{PpPs}$  and  $t_{PsPs+PpSs}$  arrival times, which can be difficult to pick if the data are noisy. Their stacking function is defined as

$$s(H, \kappa) = \sum_{i=1}^N \sum_{j=1}^3 w_j r_i(t_j), \quad (6)$$

where  $r_i(t)$  is the radial receiver function for the  $i$ th event,  $t_j(H, \kappa)$ ,  $j=1, 3$  are the predicted  $Ps$ ,  $PpPs$  and  $PpSs + PsPs$  times given by Eqs. (3)–(5), and  $w_1$ ,  $w_2$  and  $w_3$  are user-defined weights. Note that weights are assigned values such that  $\sum |w_j| = 1$ . Also,  $w_1$  and  $w_2$  are both positive, whereas  $w_3$  is negative to account for the reverse polarity of the  $PpSs + PsPs$  phase (Fig. 2a). The procedure consists of an exhaustive search of the  $H$ – $\kappa$  domain for parameters that maximize  $s$ , similar in principle to the approach used for stacking-velocity analysis in conventional seismic-reflection processing.

An example of the stacking function  $s(H, \kappa)$  for the  $N=13$  noise-free synthetic receiver functions is presented in Fig. 4a. A useful way to view this function is to note that the  $Ps$ ,  $PpPs$  and  $PpSs + PsPs$  wave pulses transform, via Eq. (6), into positive bands in the stack plot. The positive bands are centered on the corresponding kinematic curves, and maximum constructive interference occurs where these bands intersect. The elongate shape of the positive region around the maximum conveys the inherent trade-off in the resolution of  $H$  and  $\kappa$ .

Here we introduce several changes to this stacking approach. We note that the summation defined by Eq. (6) can be adversely affected by the presence of spurious noise spikes, which can lead to an erroneously large

value of  $s(H - \kappa)$  even in the absence of coherent signals. One way to suppress incoherent noise is by applying an additional weighting function based on a so-called semblance parameter, defined as

$$S_j(H, \kappa) = \frac{\left[ \sum_{i=1}^N r_i(t_j) \right]^2}{\sum_{i=1}^N r_i^2(t_j)}. \quad (7)$$

The semblance function ranges in value between zero (incoherent noise) and one (coherent signal). With semblance weighting, the stacking function becomes:

$$s'(H, \kappa) = \sum_{j=1}^3 S_j \sum_{i=1}^N w_j r_i(t_j). \quad (8)$$

Fig. 4b shows the semblance-weighted stacking function,  $s'(H, \kappa)$  for the noise-free synthetic example. Comparing this with Fig. 4a, it is evident that while both  $s$  and  $s'$  show positive regions centered on the correct parameters for the model ( $H=40$  km and  $\kappa=1.73$ ), the semblance-weighted stacking function provides sharper resolution of the peak. Figs. 4c and d show the respective stacking functions computed in the presence of random noise (noisy receiver functions in Fig. 2b). This example shows that both stacking methods perform well with moderate levels of incoherent background noise, although the semblance-weighted stacking exhibits better resolution.

Zhu and Kanamori (2000) estimated variances of  $H$  and  $\kappa$  using the first-order local approximations

$$\sigma_H^2 = 2\sigma_s / \frac{\partial^2 s}{\partial H^2} \quad (9)$$

and

$$\sigma_\kappa^2 = 2\sigma_s / \frac{\partial^2 s}{\partial \kappa^2}. \quad (10)$$

As a practical method to determine the confidence region, this approach is somewhat unsatisfactory for several reasons. First, as more events are accumulated, the functions  $s(H - \kappa)$  and  $s'(H - \kappa)$  tend to become more diffuse [i.e. smaller values of the derivatives in Eqs. (9) and (10)] due to the effects of different frequency content of signals from different events, noise and 3-D structure. Thus, the application of this method leads to the counterintuitive result that the variance of recovered parameters tends to increase as more events are stacked. Secondly, the symmetrical  $\sigma_H - \sigma_\kappa$  error ellipses produced in this manner do not adequately

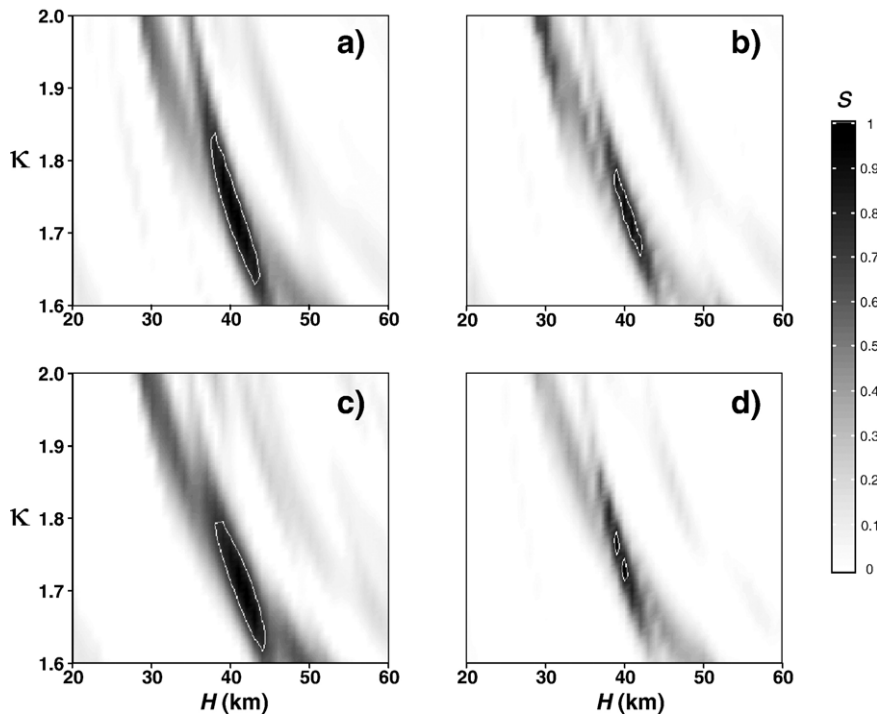


Fig. 4. Stacking functions used to determine crustal parameters. The model used to generate the synthetic seismograms is characterized by  $H=40$  km,  $\kappa=1.73$ . In each panel, the white contour encloses the standard error region. (a) Stacking function  $s(H, \kappa)$  (Eq. (6)) obtained using the synthetic receiver functions in Fig. 2a. Recovered crustal parameters are  $H=40.5 \pm 3.2$  km,  $\kappa=1.73 \pm 0.11$ . (b) Semblance-weighted stacking function  $s'(H, \kappa)$  (Eq. (8)) obtained using the synthetic receiver functions in Fig. 2a. Recovered crustal parameters are  $H=40.4 \pm 1.9$  km,  $\kappa=1.73 \pm 0.06$ . (c) Stacking function  $s(H, \kappa)$  obtained using the noisy synthetic receiver functions in Fig. 2b. Recovered crustal parameters are  $H=41.1 \pm 3.2$  km,  $\kappa=1.71 \pm 0.09$ . (d) Semblance-weighted stacking function  $s'(H, \kappa)$  obtained using the noisy synthetic receiver functions in Fig. 2b. Recovered crustal parameters are  $H=39.6 \pm 0.9$  km,  $\kappa=1.75 \pm 0.03$ .

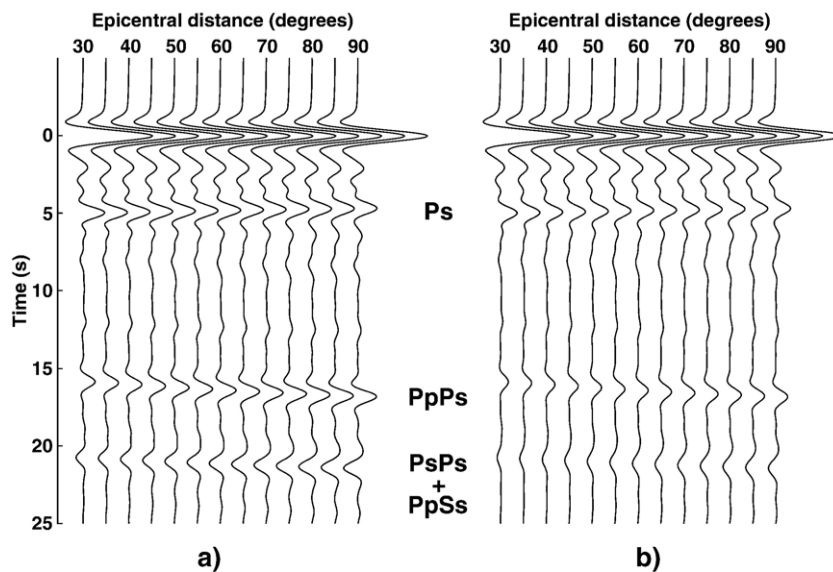


Fig. 5. Receiver functions obtained from synthetic seismograms, as in Fig. 2 but using different quality factors. (a) Elastic case,  $Q_p=Q_s=1000$  in all layers. (b) Extreme attenuation case,  $Q_p=150$ ,  $Q_s=75$  in all crustal layers,  $Q_p=Q_s=1000$  in the mantle.

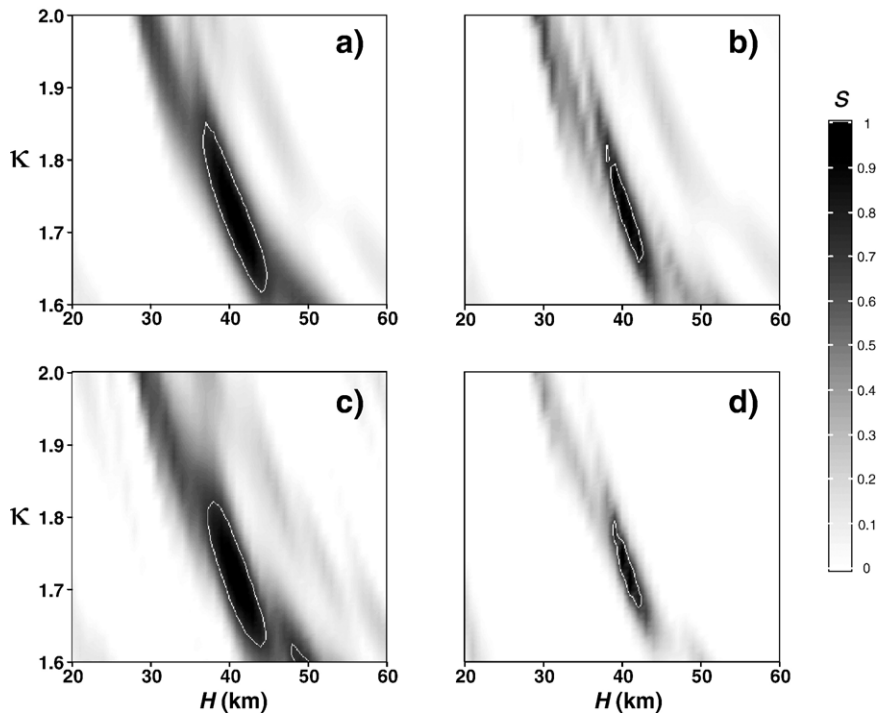


Fig. 6. Stacking functions used to determine crustal parameters, as in Fig. 4 but using the synthetic seismograms corresponding to the extreme attenuation case (Fig. 5b). (a) Stacking function  $s(H, \kappa)$  for the noise-free, high-attenuation case. Recovered parameters are  $H=40.7 \pm 4.1$  km,  $\kappa=1.73 \pm 0.12$ . (b) Semblance-weighted stacking function  $s'(H, \kappa)$  for the noise-free, high-attenuation case. Recovered crustal parameters are  $H=40.5 \pm 2.2$  km,  $\kappa=1.73 \pm 0.07$ . (c) Stacking function  $s(H, \kappa)$  for the high-attenuation case with 10% noise added. Recovered crustal parameters are  $H=40.9 \pm 3.8$  km,  $\kappa=1.72 \pm 0.10$ . (d) Semblance-weighted stacking function  $s'(H, \kappa)$  for the high-attenuation case with 10% noise added. Recovered crustal parameters are  $H=40.5 \pm 1.9$  km,  $\kappa=1.74 \pm 0.06$ .

represent the tradeoffs in parameters that are indicated by the inclined elongate contours of the stacking function.

In this paper, we estimate parameter uncertainties by constructing contours in  $s'(H, \kappa)$  that are one standard error below the maximum value, where the standard error is given by  $(\sigma^2/N)^{1/2}$ . We refer to the region(s) enclosed by the standard error contour(s) as the standard-error region. As more events are stacked, the standard-error region tends to become smaller in size. This is consistent with the notion that, for a simple scenario in which the location in the  $H$ – $\kappa$  domain of the peak value is consistent for all events, the confidence in the recovered parameters increases with the number of events stacked. The shape of the standard-error region also captures the parameter tradeoffs more naturally than a symmetrical error ellipse.

As a final synthetic data test, we have considered the effects of attenuation in the crust. This is important since the multiple reverberations ( $PpPs$ ,  $PsPs$  and  $PpSs$ ) have long crustal path lengths and are therefore sensitive to crustal  $Q$  structure. Fig. 5 compares the synthetic seismogram for a low-attenuation case, where

$Q_P=Q_S=1000$  in every layer, with a high-attenuation case where  $Q_P=150$  and  $Q_S=75$  within the crust. For the 0.5 Hz dominant frequency considered here, the synthetic results predict a 60–70% reduction in amplitude of the late-arriving multiple reverberations for the high-attenuation case. As shown in Fig. 6, both stacking methods are able to recover the crustal parameters to within uncertainty, even in the presence of moderate noise levels and high crustal attenuation. Again, the semblance-weighted stacking approach provides better resolution than the direct stacking method of Zhu and Kanamori (2000).

### 3. Data and observations

For this study, we made use of teleseismic waveforms from 71  $M > 6$  earthquakes (Table 3) that occurred between 19 February, 2003 and 9 October, 2004. The data were recorded by 32 broadband seismic stations (Fig. 1) of the POLARIS network and Canadian National Seismograph network (CNSN). Installation of the semi-portable POLARIS stations commenced in 2002 and continued until August, 2004. These stations

Table 3

List of earthquakes used in this study

Date and Time (YYYY/MM/DD_HH:MM:SS)	Latitude (deg)	Longitude (deg)	Focal depth (km)
2003/02/19_03:32:36	53.645	−164.643	19
2003/03/12_23:41:32	26.556	−110.587	10
2003/03/14_16:8:31	51.53	−173.08	33
2003/03/17_18:55:42	50.521	177.566	1.4
2003/03/17_16:36:11	50.483	177.679	7.4
2003/04/07_18:28:37	36.3	141.68	33
2003/04/11_06:12:54	7.033	−82.353	10
2003/04/24_10:56:21	48.764	154.991	43.8
2003/04/29_13:53:17	43.706	147.805	62.5
2003/05/01_00:27:4	39.007	40.464	10
2003/05/14_06:3:35	18.266	−58.633	41.5
2003/05/19_16:27:10	17.546	−105.473	10
2003/06/15_19:24:33	51.552	176.923	20
2003/06/16_22:8:2	55.492	159.999	174.8
2003/06/20_06:19:38	−7.606	−71.722	558.1
2003/06/20_13:30:41	−30.608	−71.637	33
2003/06/23_12:12:34	51.439	176.783	20
2003/07/12_23:1:38	54.65	−134.47	20
2003/07/25_22:13:29	38.415	140.996	6
2003/07/27_06:25:31	47.151	139.248	470.3
2003/07/27_11:41:27	−20.134	−65.185	345.3
2003/08/14_05:14:54	39.16	20.605	10
2003/08/31_23:8:0	43.393	132.267	481.1
2003/09/06_02:8:13	−4.623	−106.045	10
2003/09/25_19:50:6	41.815	143.91	27
2003/09/27_11:33:25	50.038	87.813	16
2003/09/27_18:52:46	50.091	87.765	10
2003/09/29_02:36:53	42.45	144.38	25
2003/10/01_01:3:25	50.211	87.721	10
2003/10/08_09:6:55	42.648	144.57	32
2003/10/28_21:48:21	43.844	147.75	65.4
2003/10/31_01:6:28	37.812	142.619	10
2003/11/05_00:58:51	4.973	−77.77	33
2003/11/12_08:26:43	33.171	137.072	384.9
2003/11/17_06:43:6	51.146	178.65	33
2003/12/09_12:44:1	51.334	−179.272	33
2003/12/22_19:15:56	35.704	−121.103	7.3
2003/12/25_07:11:11	8.416	−82.824	33
2003/12/29_01:30:54	42.423	144.613	33
2004/02/04_11:59:47	8.358	−82.877	29.2
2004/02/24_02:27:46	35.142	−3.997	0
2004/03/02_03:47:22	11.61	−86.767	28
2004/03/17_03:21:7	−21.118	−65.586	289.8
2004/03/17_05:21:0	34.583	23.323	24.5
2004/04/05_21:24:4	36.527	71.028	191.4
2004/04/14_01:54:9	55.189	162.651	51.3
2004/04/14_23:7:39	71.083	−7.601	10
2004/05/03_04:36:50	−37.695	−73.406	21
2004/05/28_12:38:44	36.249	51.622	17
2004/05/29_20:56:9	34.251	141.406	16
2004/06/10_15:19:57	55.682	160.003	188.6
2004/06/15_11:16:31	−38.854	−73.155	37.8
2004/06/28_09:49:47	54.8	−134.25	20
2004/06/29_07:1:30	10.738	−87.043	9
2004/07/11_23:8:44	30.694	83.672	13
2004/07/11_23:46:12	−20.252	−126.928	12
2004/07/15_04:27:14	−17.656	−178.76	565.5

Table 3 (continued)

Date and Time (YYYY/MM/DD_HH:MM:SS)	Latitude (deg)	Longitude (deg)	Focal depth (km)
2004/07/19_08:1:49	49.623	−126.967	23.7
2004/07/25_14:35:19	−2.427	103.981	582.1
2004/08/28_13:41:27	−34.931	−70.387	1
2004/09/03_19:4:47	−15.254	−173.34	10
2004/09/05_10:7:7	33.07	136.618	14
2004/09/05_14:57:18	33.184	137.071	10
2004/09/06_12:42:59	−55.372	−28.976	10
2004/09/06_23:29:35	33.205	137.227	10
2004/09/07_11:53:6	−28.573	−65.84	22.3
2004/09/08_14:58:25	33.14	137.2	21.2
2004/09/13_03:0:12	43.992	151.402	8
2004/09/19_20:26:4	52.214	173.951	25
2004/09/28_15:29:53	−52.438	27.985	10
2004/10/09_21:26:53	11.424	−86.633	35

are equipped with three-component Guralp CMG-ESP sensors with a flat velocity response from 100 s to 50 Hz. The two permanent CNSN stations (SADO and KGNO) used in this study are equipped with CMG-3R and CMG-3E sensors, respectively, with a flat velocity response from 130 s to 30 Hz. POLARIS broadband data are sampled at 100 Hz, whereas the CNSN broadband data are sampled at 40 Hz.

For all  $M > 6$  events in the epicentral distance range  $30^\circ \leq \Delta \leq 100^\circ$  during the time interval for this study, we extracted 1 h of data starting from the origin time of the event. Using IASP91 arrival time information, we verified the quality of the  $P$  arrival using the vertical channel, and adjusted the  $P$  time pick if necessary. For events with a clear  $P$  arrival we extracted 3-component waveform data, for a time window starting 30 s before and ending 100 s after the  $P$  time pick. Receiver functions were computed using Eqs. (1) and (2), with a water-level parameter  $c = 0.05$  and Gaussian filter parameters  $\omega_0 = 0.2\pi$  Hz and  $\sigma_0 = 0.4$  Hz. Receiver functions were then inspected and those with low signal/noise ratio (SNR) were rejected. The number of remaining high-quality events used for each station (Table 4) varies from 4 to 34, depending on the length of the recording period and background noise level at the station.

A final data inspection was performed by stacking receiver functions for each station. This simple stacking procedure reduces noise and eliminates variations caused by 3-D structure, so that the summed response reflects the average structure. Fig. 7 shows a profile constructed by arranging 10 of the stacked receiver functions sequentially, from southeast to northwest. This profile (SE–NW, Fig. 1) extends 520 km across the Grenville orogen. The Moho  $P_s$  converted phase exhibits



Table 4  
List of seismograph stations and measured parameters

Station	Latitude (deg)	Longitude (deg)	Seismograph network <sup>a</sup>	$N^b$	$H$	$H_{\text{err}}^c$	$\kappa$	$\kappa_{\text{err}}^c$
ACTO	43.6087	−80.0624	POLARIS	25	40.5	0.9	1.77	0.04
ALFO	45.6283	−74.8842	POLARIS	18	37.0	0.5	1.80	0.02
ALGO	45.9544	−78.0509	POLARIS	32	43.0	0.5	1.81	0.02
BANO	45.0198	−77.928	POLARIS	19	40.0	0.4	1.74	0.01
BRCO	44.2437	−81.4422	POLARIS	11	45.0	0.4	1.78	0.01
BUKO	45.4423	−79.399	POLARIS	8	40.5	1.0	1.77	0.03
CBRQ	47.3092	−76.4707	POLARIS	3	34.5	0.9	1.73	0.05
CLPO	45.246	−76.9642	POLARIS	12	39.0	0.6	1.76	0.02
CLWO	44.4491	−80.3013	POLARIS	19	42.5	1.7	1.79	0.06
DELO	44.5177	−77.6186	POLARIS	23	39.0	0.5	1.78	0.01
ELGO	43.6755	−80.4374	POLARIS	27	43.0	1.4	1.74	0.04
HGVO	42.9607	−80.1264	POLARIS	19	40.9	0.5	1.77	0.01
KGNO	44.2272	−76.4934	CNSN	12	40.1	0.4	1.83	0.01
KLBO	45.3566	−80.2132	POLARIS	9	43.5	0.9	1.85	0.03
KSVO	44.5524	−73.6861	POLARIS	10	36.5	1.0	1.80	0.05
LINO	44.3541	−78.7802	POLARIS	18	39.0	0.4	1.73	0.01
MEDO	43.1646	−78.4546	POLARIS	7	41.9	0.5	1.75	0.01
MPPO	44.77	−76.2648	POLARIS	21	40.5	0.9	1.73	0.03
MRHQ	45.887	−74.2127	POLARIS	4	38.2	1.3	1.72	0.05
PECO	43.934	−76.9939	POLARIS	19	44.0	0.5	1.74	0.01
PEMO	45.6773	−77.2466	POLARIS	25	37.9	0.5	1.74	0.02
PKRO	43.9643	−79.0714	POLARIS	23	40.0	0.5	1.73	0.01
PLIO	41.7505	−82.6284	POLARIS	16	52.4	1.7	1.73	0.07
PLVO	45.0396	−77.0754	POLARIS	11	38.6	1.0	1.77	0.04
PTCO	42.8844	−79.3115	POLARIS	18	43.5	1.0	1.74	0.02
RSPO	46.0734	−79.7602	POLARIS	7	36.5	1.0	1.74	0.04
SADO	44.7694	−79.1417	CNSN	18	38.0	0.5	1.74	0.01
STCO	43.2096	−79.1705	POLARIS	17	43.0	0.5	1.72	0.01
SUNO	46.6438	−81.3442	POLARIS	17	36.0	0.5	1.69	0.02
TOBO	45.2257	−81.5234	POLARIS	14	39.5	0.9	1.75	0.02
TYNO	43.095	−79.8702	POLARIS	21	40.5	0.9	1.79	0.03
WLVO	43.9236	−78.397	POLARIS	34	40.5	0.8	1.73	0.02

$H$  denotes crustal thickness (km);  $\kappa$  denotes  $V_p/V_s$  ratio.

<sup>a</sup> POLARIS denotes stations operated by the POLARIS consortium (Portable Observatories for Lithospheric Analysis and Research Investigating Seismicity); CNSN denotes Canadian National Seismograph Network.

<sup>b</sup> Number of events used in the analysis.

<sup>c</sup> Uncertainties are measured using the standard error contour in plots of semblance-weighted stacking function.

considerable variability in time ( $4.5 \leq t_{Ps} \leq 6.0$  s), including a pronounced downward deflection at station KLBO, about 90 km SE of the Grenville Front. A Moho trough has been observed in seismic-refraction studies (Winardhi and Mereu, 1997) and receiver-function analysis (Rondenay et al., 2000) along a corridor located about 150 km east of this profile, near stations BANO and ALGO (Fig. 1). Rondenay et al. (2000) also observed a north-dipping upper mantle event, similar to the dashed event marked in Fig. 7, which they interpreted as a relict subduction zone.

Crustal thickness and  $V_p/V_s$  ratio were analyzed using the stacking methods described by Eqs. (7) and (8). Figs. 8 and 9 illustrate typical analyses, for stations ACTO and PEMO, respectively. All stacks were performed using a fixed average  $P$ -wave velocity of

6.39 km/s, derived from the velocity model in Table 2. The weighting function ( $w$ ) was adjusted interactively for each station to provide the best resolution of crustal parameters. In most cases, we found the best results were achieved with  $w_2 > w_1 > w_3$ . This scheme arises because the multiple reverberations associated with  $w_2$  ( $PpPs$ ) and  $w_3$  ( $PsPs + PpSs$ ) are considerably weaker in amplitude than the Moho event, and thus tend to be overpowered in the stacking function. This effect is compensated by setting  $w_2 > w_1$ . Due to the typically low SNR of the  $PsPs + PpSs$ , it was generally assigned a low weight in the stack.

Fig. 10 shows the Moho structure and  $\kappa$  ( $V_p/V_s$ ) values obtained along the 1992 LITHOPROBE line MDG, which passes through part of our seismograph network. The smoothed  $\kappa$  data were obtained from the refraction

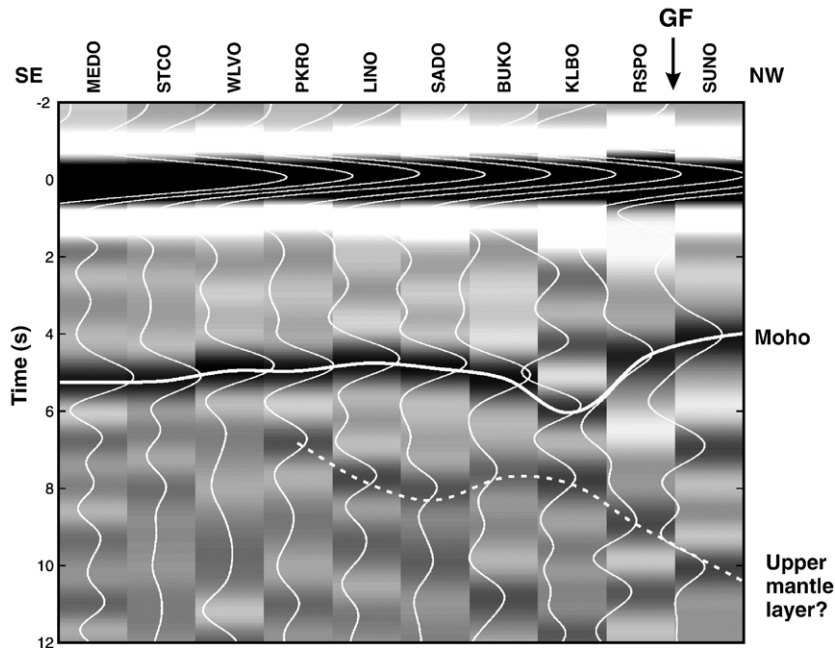


Fig. 7. Stacked receiver-function profile across the Grenville orogen, presented as wiggle traces superimposed on a variable-density background. The profile is approximately 520 km in length. The Moho is indicated by the smooth curve passing through the Moho  $P_s$  converted phase on each receiver function. A downward deflection of the Moho and upper-mantle layer, similar to those seen here, were observed by Rondenay et al. (2000) in a receiver-function profile located 150 km east of this profile. GF denotes Grenville Front, the northeastern limit of the Grenville orogen. See Fig. 1 for profile location.

observations by binning 6220 direct  $V_p/V_s$  measurements, as described above, into 10-km-wide bins. The data in each bin is plotted in the lower half of Fig. 10; error bars are 2 standard deviations in length. This figure clearly shows that the rocks of the Grenville Province have a higher  $V_p/V_s$  ratio than those north of the Front. A similar result was obtained by Mereu (2000). It is difficult to make a direct comparison with the receiver-function data from this study, as the POLARIS stations do not lie exactly along line MDG but cover the region in a 2-D areal sense. Since the Moho trough south of the Grenville Front and the dramatic change in the  $V_p/V_s$  ratio across the Front appear to be associated with the tectonic structure of the region, we have chosen to compare the results of these 2 independent studies by plotting the receiver-function results for stations PECO, DELO, BANO, ALGO, KGNO, WLVO, PLVO, PEMO and RSPO as star symbols on Fig. 10. For plotting purposes, the location of POLARIS stations was determined based on distance from the Grenville Front. Fig. 10 shows that there is a very good agreement between the  $H$  and  $\kappa$  values from this study with those obtained from the 1992 LITHOPROBE refraction experiment. We note that the scatter in the teleseismic  $\kappa$  values is similar to the

scatter in individual measurements of  $V_p/V_s$  from the refraction data.

Fig. 11 shows a cross-plot of crustal thickness obtained from seismic refraction measurements (Table 1), versus the crustal-thickness estimates from this study (including those used in Fig. 10). We find overall good agreement between the two types of estimates; for example, the all stations but KGNO that are located within 30 km (approximately one crustal thickness) from a refraction profile agree to within 7% of the refraction-derived crustal thickness. Differences between the refraction and teleseismic measurements of crustal thickness could arise because: 1) differences in structure between the seismic station and the nearest refraction profile; 2) variations in  $P$ -wave velocity from the assumed average value of 6.39 km/s will produce errors in crustal thickness that are not accounted for in the uncertainty method used here; 3) the Moho imaged with refraction methods (frequencies of 1–10 Hz) may not coincide with the Moho evident from teleseismic analysis (centre frequency of 0.4 Hz).

A map of crustal thickness derived from the analysis of 31 of the stations is shown in Fig. 12a. The contour map was produced by interpolating the  $H$  observations onto an evenly sampled grid with a spacing of  $0.2^\circ$  in

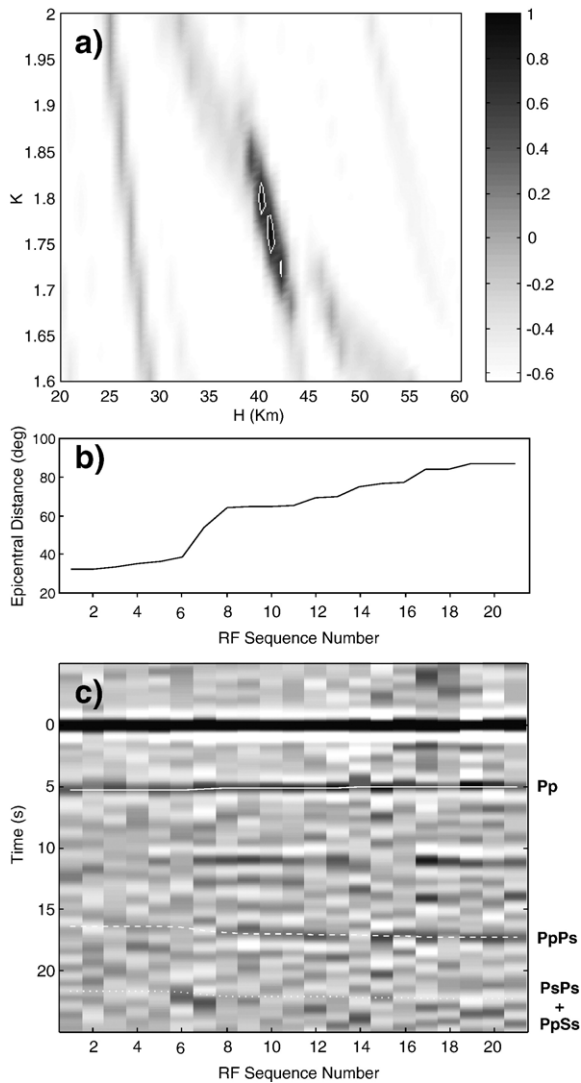


Fig. 8. (a) The semblance-weighted stack  $s'(H, \kappa)$  for station ACTO. The white contour encloses the standard error region. The recovered crustal parameters are  $H = 40.5 \pm 0.9$  km and  $\kappa = 1.79 \pm 0.04$ . (b) Epicentral distances of the events used in the analysis. (c) Receiver-function (RF) profile, showing the predicted arrival times of the  $Ps$ ,  $PpPs$  and  $PsPs + PpSs$  phases based on the recovered crustal parameters. The profile consists of the 21 receiver functions used to obtain (a), displayed as variable density images and arranged by increasing epicentral distance.

both longitude and latitude, using a triangular-based linear interpolation algorithm. Note that we have excluded station PLIO, located at the extreme southwest corner of our network on Pelee Island in Lake Erie, from the gridding procedure. PLIO yielded an unusual crustal thickness of  $52.4 \pm 1.7$  km (see Table 3), significantly thicker than observed elsewhere in our network. The relative isolation of PLIO coupled with the anomalous

crustal thickness conspired to produce an unrealistic distortion of the contours in our automatic gridding procedure. As discussed below, we believe that the extreme thickness of the crust at PLIO is related to its location within the mid-continent rift system. Fig. 12b shows a crustal thickness map produced in the same manner, but including refraction-based crustal thickness values at the control points indicated in Fig. 1. The two maps are nearly identical, providing additional evidence

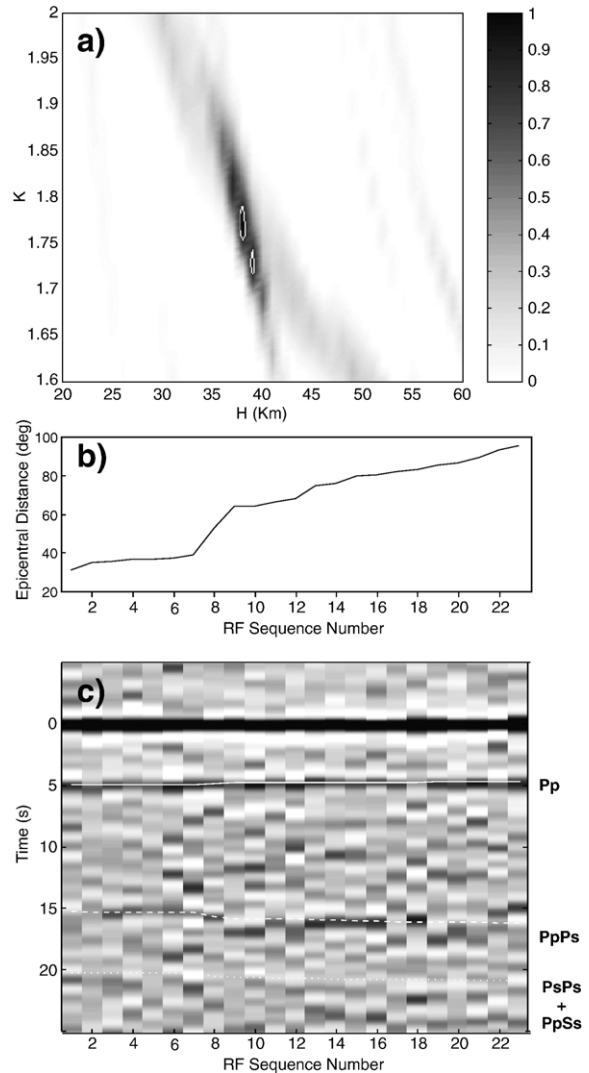


Fig. 9. (a) The semblance-weighted stack  $s'(H, \kappa)$  for station PEMO. The white contour encloses the standard error region. The recovered crustal parameters are  $H = 37.9 \pm 0.5$  km and  $\kappa = 1.73 \pm 0.02$ . (b) Epicentral distances of the events used in the analysis. (c) Receiver-function (RF) profile, showing the predicted arrival times of the  $Ps$ ,  $PpPs$  and  $PsPs + PpSs$  phases based on the recovered crustal parameters. The profile consists of the 23 receiver functions used to obtain (a), displayed as variable density images and arranged by increasing epicentral distance.

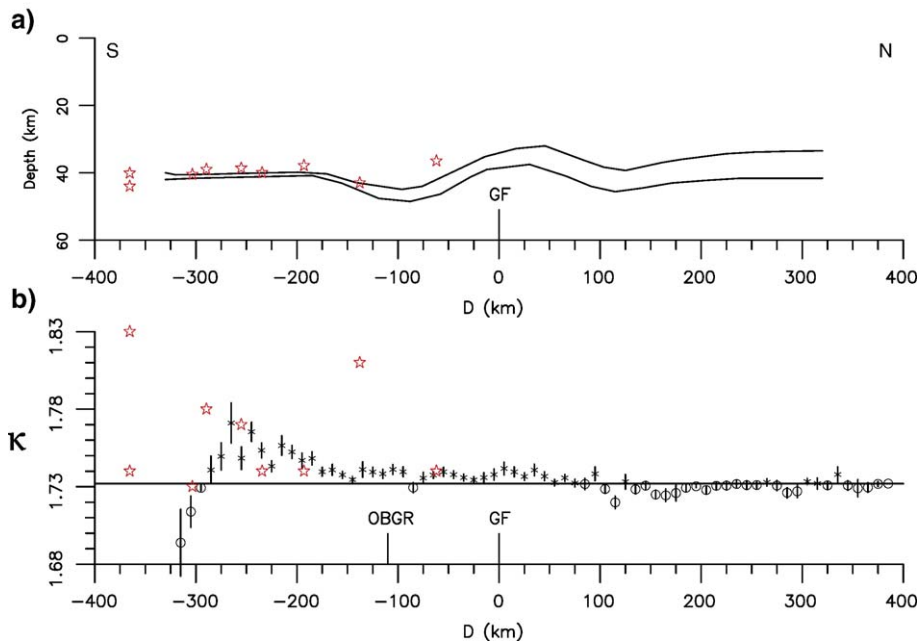


Fig. 10. Moho structure (a) and the smoothed variation of  $V_p/V_s$  ( $\kappa$ ) ratios (b) along LITHOPROBE Line MDG (Fig. 1). Values derived from teleseismic analysis (stations PECO, DELO, BANO, ALGO, KGNO, WLVO, PLVO, PEMO, and RSPO) are shown as stars. The crustal thickness estimates obtained using these two independent methods show good agreement. The two curves in (a) delineate the Moho transition zone (Winardhi and Mereu, 1997). GF denotes Grenville Front.

that the teleseismic and refraction-based crustal thickness estimates are mutually consistent. In general, the crustal thickness values and associated trends are in good agreement with results obtained in a recent continental-scale synthesis (Chulick and Mooney, 2002).

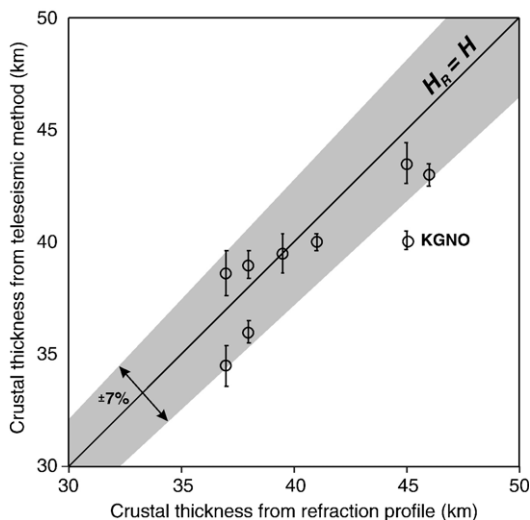


Fig. 11. Comparison between crustal thickness based on published refraction profiles and the crustal thickness from this study. The graph shows stations located within 35 km of a refraction line.

Fig. 13 shows maps of  $V_p/V_s$  ratio ( $\kappa$ ) produced using the same gridding procedure as for the crustal thickness maps in Fig. 12. Compared with the map obtained with the teleseismic results alone (Fig. 13a), the inclusion of refraction data (Fig. 13b) produces little change. However, linear contouring artifacts that coincide with the locations of refraction profiles indicate small discrepancies between the two methods. We attribute these discrepancies to two main factors. First, due to the shape of the error ellipse in the stacking diagrams (Figs. 8 and 9),  $\kappa$  is less well constrained than  $H$  by our receiver-function method. This tendency is also manifested in the scatter of  $\kappa$  values evident in the lower panel of Fig. 10. Secondly, whereas the teleseismic method yields an average  $\kappa$  for the crust, for the refraction measurements most of the data points are from  $P_g$  and  $S_g$  arrivals that sample only the upper 20 km. The refraction measurements therefore contain a slight bias toward lower values of  $\kappa$ , which characterizes the felsic upper crust (Musacchio et al., 1997).

#### 4. Discussion

The maps of crustal thickness and  $V_p/V_s$  ratio are divisible into 3 distinct regions that appear to correlate with surface geology. Referring to Figs. 12 and 13,



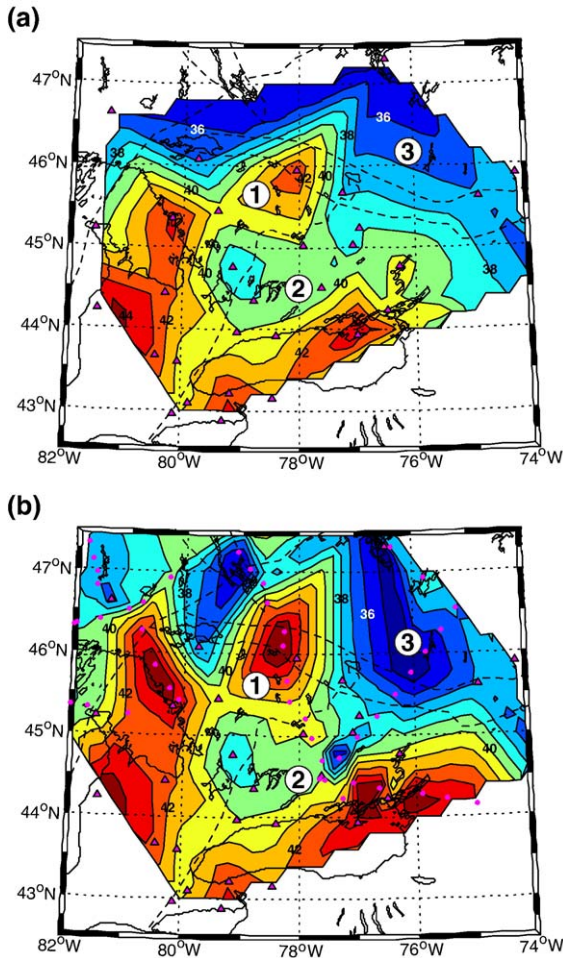


Fig. 12. (a) Crustal thickness ( $H$ ) map derived from the teleseismic analysis, excluding station PLIO. Triangles show the locations of seismograph stations. Dashed lines show geological boundaries from Fig. 1. Area 1 denotes a region of relatively thick crust and high  $\kappa$  value, which occurs within the high-grade Central Gneiss Belt. Area 2 denotes a region of intermediate-thickness crust and low  $\kappa$  value within the medium-grade Composite Arc Terrane. Area 3 denotes a region of thin crust east of the Ottawa–Bonnechere graben. (b) Crustal-thickness map produced using both teleseismic results (this study) and compiled refraction data. Circles show location of refraction control points. Contours are in km. Contour interval is 1 km.

region 1 is an area of relatively thick crust (40–44 km) and relatively high  $\kappa$  value ( $>1.78$ ). This area falls within the Central Gneiss Belt (CGB) of the Grenville Province, a terrane where high-grade (generally granulite facies) gneisses and migmatites are exposed, including areas where relict eclogite-facies assemblages occur within mafic enclaves (Carr et al., 2000). Current models for the tectonic evolution of the Grenville orogeny (Rivers, 1997) suggest that much of the CGB

was exhumed from mid- to lower-crustal levels. The higher  $\kappa$  values in this area are consistent with a more mafic composition typical of lower crustal assemblages (Holbrook et al., 1992). Region 2 is an area of intermediate crustal thickness (37–39 km) and low  $\kappa$  value ( $<1.75$ ). This region is located within the Composite Arc Terrane (CAT), within which near-surface belts comprise moderate to low-grade supra-crustal rocks that accreted to the margin of Laurentia and were intruded by granitoid plutons (Carr et al., 2000). Although the CGB is interpreted to continue in the lower crust beneath the CAT for up to  $\sim 100$  km (White et al., 2000), we infer that the greater thickness of high-

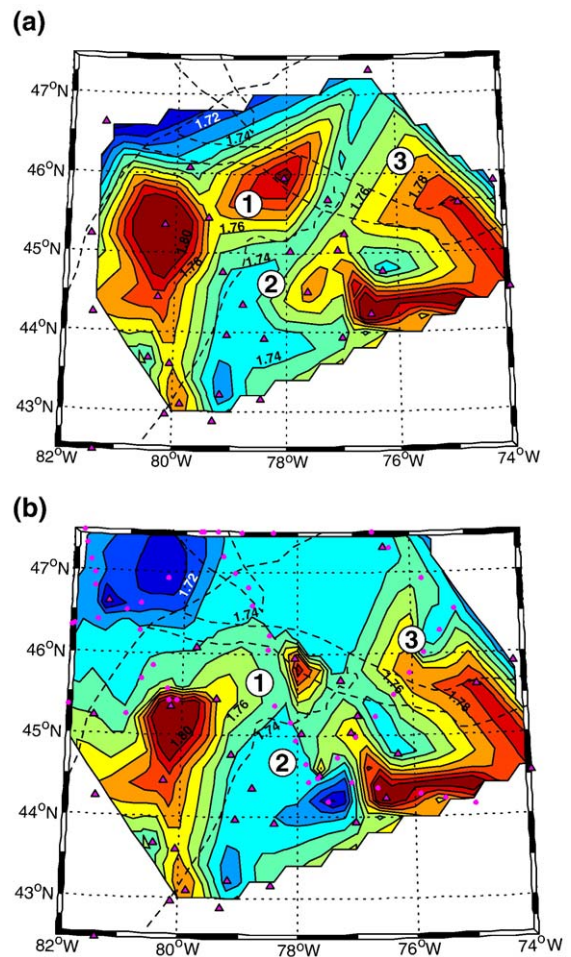


Fig. 13. (a) Map of  $V_p/V_s$  ratio ( $\kappa$ ) derived from the teleseismic analysis, excluding station PLIO. Triangles show the locations of seismograph stations. Dashed lines show geological boundaries from Fig. 1. Numbers indicated interpreted domains of distinct crustal thickness and  $\kappa$  value, as in Fig. 10. (b) Map of  $V_p/V_s$  ratio ( $\kappa$ ) produced using both teleseismic results (this study) and compiled refraction data.

grade crust within the CGB relative to CAT is sufficient to influence bulk crustal  $\kappa$  value. Indeed, there is a remarkable similarity between the boundary between regions 1 and 2, as implied by the  $\kappa=1.75$  contour in Fig. 13, and the tectonic boundary separating CAT and CGB (the Central Metasedimentary Belt boundary tectonic zone; Fig. 1). Farther southeast, crustal thickening beneath Lake Ontario coincides approximately with the southeastern boundary of CAT. Finally, region 3 is an area of thin crust ( $<38$  km) and variable  $V_P/V_S$  ratio. This area is entirely located northeast of the Ottawa–Bonnechere graben, a post-Grenvillian extensional feature that formed during the opening of the Iapetus ocean (ca. 0.7 Ga; Kamo et al., 1995). It is interesting to note that region 3 appears to coincide with the Western Quebec Seismic Zone (Fig. 14), an area of relatively intense intraplate seismicity.

Although the unusually thick crust beneath station PLIO posed difficulties for our automatic contouring algorithm, very thick crust at this location is consistent with other studies. Based on drill-core data and potential-field anomaly maps, the mid-continent rift is believed to extend at least as far as the western end of Lake Erie (Easton and Carter, 1995) near station PLIO. Moreover, the existence of a thick crustal root beneath the midcontinent rift has been known since the 1963 Lake Superior seismic experiment (Berry and West, 1966; Smith et al., 1966) and is readily apparent in the most recent global model for crustal thickness (CRUST2.1; Fig. 15).

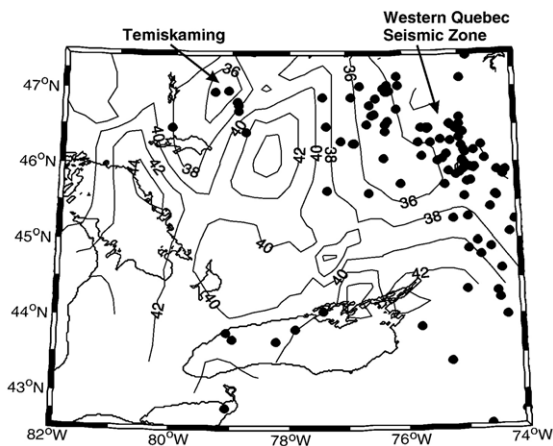


Fig. 14. Comparison between crustal thickness and regional seismicity. Dots show earthquakes epicentres ( $M_N \geq 3.0$ ) for events between 1990/01/01 and 2005/01/15. Crustal thickness contours are in km and are based on both teleseismic and refraction results. Note that the most seismically active regions, the Western Quebec Seismic Zone (Forsyth, 1981) and the Temiskaming area, are located in the areas of relatively thin crust ( $<38$  km).

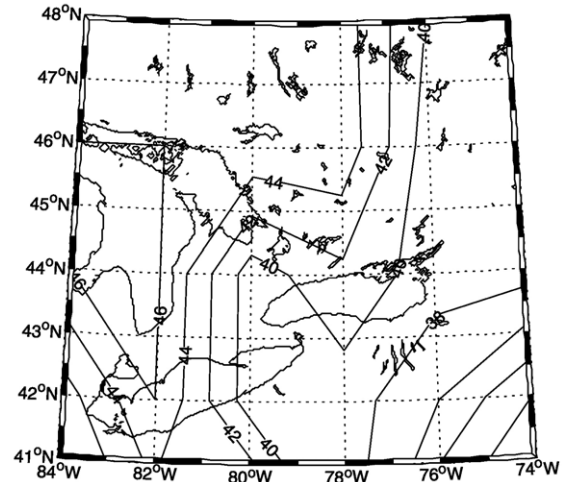


Fig. 15. Crustal thickness map produced using Crust 2.0 (Bassin et al., 2000), the highest-resolution global model for crustal thickness that is currently available.

We remark that the variation in crustal thickness apparent in our data is far in excess of that required for simple local Airy isostatic equilibrium. For example, we observe  $>18.0$  km of crustal thickness variation; a simple airy-type isostatic calculation using a Moho density contrast of  $300 \text{ kg/m}^3$  and a surface density contrast of  $2670 \text{ kg/m}^3$  implies surface relief of up to 2 km, whereas the surface elevation over the study region varies by  $<1.0$  km and in most places is  $<400$  m. Furthermore, there is no significant surface topographic expression of the areas of thickened crust in our model. It is possible that this apparent decoupling of crustal thickness variations and surface relief is due to partial eclogitization of the lowermost crust, which tends to reduce the relative buoyancy of lower crustal roots beneath ancient mountain belts (Fischer, 2002; Eaton, 2006). Even without appealing to eclogitization, variations in the proportions of mafic and felsic rock in the crustal columns of the CGB and CAT may partly explain observed variations in crustal thickness (Figs. 12 and 13).

## 5. Conclusions

The use of semblance weighting in the receiver-function stacking method developed by Zhu and Kanamori (2000) leads to reduced uncertainties in point estimates of crustal thickness ( $H$ ) and  $V_P/V_S$  ratio ( $\kappa$ ). We have applied this technique to 32 broadband seismograph stations, most of which have been installed since 2001 as part of the POLARIS project. This broadband seismograph network covers a

$\sim 700 \times 400 \text{ km}^2$  segment of the central Grenville orogen, in the lower Great Lakes region of eastern North America. Despite the simplified treatment of the crust as a single homogeneous layer that is implicit in our method,  $H$  and  $\kappa$  derived from the teleseismic analysis are in good agreement with those obtained from previous large-scale refraction experiments. The coverage afforded by the seismograph network and refraction profiles enables us to develop well-constrained maps of  $H$  and  $\kappa$ , which reveal a number of distinct domains. The crustal thickness variations show a strong correlation with surface geological belts, but do not correlate with surface topography and exceed the relief required to maintain local isostatic equilibrium. Domains such as the Central Gneiss Belt, where rocks have been exhumed from mid-to-lower crustal levels, show a higher  $V_p/V_s$  ratio than other areas. This observation is consistent with the more mafic composition of the lower crust. An area of thin crust northeast of the Ottawa–Bonnechere graben appears to correlate with a zone of high intraplate seismicity, suggesting a possible causal relationship.

## Acknowledgments

This study would not have been possible without the exceptional work of Isa Asudeh, Bernie Dunn and Kadircan Aktas to install, maintain and operate the POLARIS network. Funding for the POLARIS network in Ontario has been provided by Ontario Power Generation, Bruce Power, the Canada Foundation for Innovation and the Ontario Innovation Trust fund. Operational support has been provided by the Natural Sciences and Engineering Research Council of Canada and the Ontario Research and Development Trust Fund. Data for all stations are archived by the Geological Survey of Canada and are available online at <http://seismo.nrcan.gc.ca>. Earthquake epicenters in Fig. 14 were obtained from the Earthquakes Canada online bulletin at <http://www.seismo.nrcan.gc.ca/nedb/bulle.php>. The manuscript benefited from constructive reviews by Andrew Hynes, Walter Mooney and Chuck Hurich.

## References

- Atkinson, G., Adams, J., Asudeh, I., Bostock, M., Cassidy, J., Eaton, D., Ferguson, I., Jones, A., Snyder, D., White, D., 2003. POLARIS update: fall 2002. *Seismol. Res. Lett.* 74, 41–43.
- Bassin, C., Laske, G., Masters, G., 2000. The current limits of resolution for surface wave tomography in North America. *EOS Trans. Am. Geophys. Union* 81, 897.
- Bath, M., Steffanson, R., 1966. S–P conversions from the base of the crust. *Ann. Geophys.* 19, 119–130.
- Berry, M.J., Fuchs, K., 1973. *Bull. Seismol. Soc. Am.* 63, 1393–1432.
- Berry, M.J., West, G.F., 1966. An interpretation of the first arrival data of the Lake Superior experiment by the time-term method. *Bull. Seismol. Soc. Am.* 56, 141–171.
- Boland, A.V., Ellis, R.M., 1989. Velocity structure of the Kapuskasing uplift. *J. Geophys. Res.* 94, 7189–7284.
- Bostock, M.G., Cassidy, J.F., 1995. The upper mantle discontinuities in western Canada from Ps conversions. *Pure Appl. Geophys.* 145, 219–234.
- Carr, S.D., Easton, R.M., Jamieson, R.A., Culshaw, N.G., 2000. Geologic transect across the Grenville orogen of Ontario and New York. *Can. J. Earth Sci.* 27, 193–216.
- Chulick, G.S., Mooney, W.D., 2002. Seismic structure of the crust and uppermost mantle of North America and adjacent oceanic basins: a synthesis. *Bull. Seismol. Soc. Am.* 92, 2478–2492.
- Dineva, S., Eaton, D., Mereu, R., 2004. Seismicity of the Southern Great Lakes: revised earthquake hypocenters and possible tectonic controls. *Bull. Seismol. Soc. Am.* 94, 1902–1918.
- Easton, R.M., Carter, T.R., 1995. Geology of the Precambrian basement beneath the Paleozoic of southwestern Ontario. In: Ojakangas, R.W., et al. (Eds.), *Basement Tectonics*, vol. 10, pp. 221–264.
- Eaton, D., 2006. Multi-genetic origin of the continental Moho: insights from Lithoprobe. *Terra Nova* 18, 34–43.
- Eaton, D., Hope, J., 2003. Structure of the crust and upper mantle of the Great Slave Lake shear zone, NWT, from Teleseismic Analysis and Gravity Modelling. *Can. J. Earth Sci.* 40, 1203–1218.
- Fischer, K.M., 2002. Waning buoyancy in the crustal roots of old mountains. *Nature* 417, 933–935.
- Forsyth, D.A., 1981. Characteristics of the Western Québec Seismic Zone. *Can. J. Earth Sci.* 18, 103–119.
- Grandjean, G., Wu, H., White, D., Mareschal, M., Hubert, C., 1995. Crustal velocity models for the Archean Abitibi greenstone belt from seismic refraction data. *Can. J. Earth Sci.* 32, 149–166.
- Green, A.G., Milkereit, B., Davidson, A., Spencer, C., Hutchinson, D.R., Cannon, W.F., Lee, M.W., Agena, W.F., Behrendt, J.C., Hinze, W.J., 1988. Crustal structure of the Grenville Front and adjacent terranes. *Geology* 16, 788–792.
- Hodgson, J.H., 1953. A seismic survey in the Canadian Shield: I. Refraction studies based on rockbursts at Kirkland Lake, Ontario. *Publ. Dom. Obs. Ott.* 16, 113–163.
- Holbrook, W.S., Mooney, W.D., Christensen, N.I., 1992. The seismic velocity structure of the deep continental crust. In: Fountain, D.M., Arculus, R., Kay, R.W. (Eds.), *Continental Lower Crust*. Elsevier Science Publ. Co., Oxford.
- Hughes, S., Luetgert, J.H., 1992. Crustal structure of the southeastern Grenville Province, northern New York State and eastern Ontario. *J. Geophys. Res.* 97, 17455–17479.
- Kamo, S.L., Krogh, T.E., Kumarapeli, P.S., 1995. Age of the Grenville dyke swarm, Ontario–Quebec: implications for the timing of Iapetan rifting. *Can. J. Earth Sci.* 32, 273–280.
- Karlstrom, K.E., Harlan, S.S., Williams, M.L., McLelland, J., Geissman, J.W., Ahall, K.-I., 1999. Redefining Rodinia: geological evidence for the Australia–western U.S. connection in the Proterozoic. *GSA Today* 9 (10), 1–7.
- Kennett, B.L.N., Engdahl, E.R., 1991. Travel times for global earthquake location and phase identification. *Geophys. J. Int.* 105, 429–465.
- Langston, C.A., 1977. The effect of planar dipping structure on source and receiver responses for constant ray parameter. *Bull. Seismol. Soc. Am.* 67, 1029–1050.



- Long, C., Salisbury, M.H., 1996. The velocity structure of the Britt Domain, southwestern Grenville Province, from laboratory and refraction experiments. *Can. J. Earth Sci.* 33, 729–744.
- Ludden, J., Hynes, A., 2000. The Lithoprobe Abitibi–Grenville transect: two billion years of crust formation and recycling in the Precambrian Shield of Canada. *Can. J. Earth Sci.* 37, 459–476.
- Mereu, R.F., 2000. The complexity of the crust and Moho under the southeastern Superior and Grenville provinces of the Canadian Shield from seismic refraction – wide-angle reflection data. *Can. J. Earth Sci.* 37, 439–458.
- Mereu, R.F., Jobidon, G., 1971. A seismic investigation of the crust and Moho on a line perpendicular to the Grenville Front. *Can. J. Earth Sci.* 8, 1553–1583.
- Mereu, R.F., Wang, D., Kuhn, O., Forsyth, D.A., Green, A.G., Morel, P., Buchbinder, G.G.R., Crossley, D., Schwarz, E., duBerger, R., Brooks, C., Clowes, R., 1986. The 1982 COCRUST seismic experiment across the Ottawa–Bonnetiere graben and Grenville Front in Ontario and Quebec. *Geophys. J. R. Astr. Soc.* 84, 491–514.
- Mereu, R.F., Epili, D., Green, A.G., 1991. Pg shingle; preliminary result from the onshore Glimpsee refraction experiment. *Tectonophysics* 173, 617–626.
- Mooney, W., Laske, G., Masters, T.G., 1998. Crust 5.1: a global crustal model at  $5 \times 5$  degrees. *J. Geophys. Res.* 103, 727–747.
- Musacchio, G., Mooney, W.D., Luetgert, J.H., 1997. Composition of the crust in the Grenville and Appalachian provinces of North America inferred from  $V_p/V_s$  ratios. *J. Geophys. Res.* 102, 15225–15241.
- O'Dowd, C.R., Eaton, D., Forsyth, D., Asmis, H.W., 2004. Structural fabric of the Central Metasedimentary Belt, Canada, from deep seismic profiling. *Tectonophysics* 388, 145–159.
- Owens, T.J., Zandt, G., Taylor, S.R., 1984. Seismic evidence for ancient rift beneath the Cumberland Plateau, Tennessee: a detailed analysis of broadband teleseismic P waveforms. *J. Geophys. Res.* 89, 7783–7795.
- Rivers, T., 1997. Lithotectonic elements of the Grenville Province: review and tectonic implications. *Precambrian Res.* 86, 117–154.
- Rondenay, S., Bostock, M., Hearn, G., White, D., Ellis, R., 2000. Lithospheric assembly and modification of the SE Canadian Shield: Abitibi–Grenville teleseismic experiment. *J. Geophys. Res.* 105, 13735–13754.
- Smith, T.J., Steinhart, J.S., Aldrich, L.T., 1966. Lake Superior crustal structure. *J. Geophys. Res.* 4, 1141–1172.
- Wang, R., 1999. A simple orthonormalization method for stable and efficient computation of Green's functions. *Bull. Seismol. Soc. Am.* 89, 741–760.
- White, D.J., Forsyth, D., Asudeh, I., Carr, S.D., Wu, H., Easton, R.M., Mereu, R.F., 2000. A seismic-based cross-section of the Grenville Orogen in southern Ontario and western Quebec. *Can. J. Earth Sci.* 37, 183–192.
- Winardhi, S., Mereu, R.F., 1997. Crustal velocity structure of the Superior and Grenville provinces of the southeastern Canadian Shield. *Can. J. Earth Sci.* 34, 1167–1184.
- Zandt, G., Ammon, C.J., 1995. Continental–crust composition constrained by measurements of crustal Poisson's ratio. *Nature* 374, 152–154.
- Zandt, G., Myers, S.C., Wallace, T.C., 1995. Crust and mantle structure across the Basin and range – Colorado Plateau boundary at  $37^\circ\text{N}$  latitude and implications for Cenozoic extensional mechanism. *J. Geophys. Res.* 100, 10529–10548.
- Zelt, C.A., Forsyth, D.A., Milkereit, B., White, D.J., Asudeh, I., Easton, R.M., 1994. Seismic structure of the Central Metasedimentary belt, southern Grenville province. *Can. J. Earth Sci.* 31, 243–254.
- Zhu, L., Kanamori, H., 2000. Moho depth variation in southern California from teleseismic receiver functions. *J. Geophys. Res.* 105, 2969–2980.